Ultramicroscopy 110 (2010) 134–143

Contents lists available at ScienceDirect

Ultramicroscopy

journal homepage: www.elsevier.com/locate/ultramic

Multivariate statistics applications in phase analysis of STEM-EDS spectrum images

Chad M. Parish *,1, Luke N. Brewer

Sandia National Laboratories, Albuquerque, NM 87185, USA

ARTICLE INFO

Article history:
Received 26 February 2009
Received in revised form
28 September 2009
Accepted 13 October 2009

Keywords:
STEM
X-ray microanalysis
Spectrum imaging
Spectral imaging
Quantification
Multivariate statistical analysis
Principal component analysis
PCA

ABSTRACT

Spectrum imaging (SI) methods are displacing traditional spot analyses as the predominant paradigm for spectroscopic analysis with electron beam instrumentation. The multivariate nature of SI provides clear advantages for qualitative analysis of multiphase specimens relative to traditional gray-scale images acquired with non-spectroscopic signals, where different phases with similar average atomic number may exhibit the same intensity. However, with the improvement in qualitative analysis with the SI paradigm has come a decline in the quantitative analysis of the phases thus identified, since the spectra from individual pixels typically have insufficient counting statistics for proper quantification. The present paper outlines a methodology for quantitative analysis within the spectral imaging paradigm, which is illustrated through X-ray energy-dispersive spectroscopy (EDS) of a multiphase (Pb,La)(Zr,Ti)O_3 ceramic in scanning transmission electron microscopy (STEM). Statistical analysis of STEM-EDS SI is shown to identify the number of distinct phases in the analyzed specimen and to provide better segmentation than the STEM high-angle annular dark-field (HAADF) signal. Representative spectra for the identified phases are extracted from the segmented images with and without exclusion of pixels that exhibit spectral contributions from multiple phases, and subsequently quantified using Cliff–Lorimer sensitivity factors. The phase compositions extracted with the method while excluding pixels from multiple phases are found to be in good agreement with those extracted from user-selected regions of interest, while providing improved confidence intervals. Without exclusion of multiphase pixels, the extracted composition is found to be in poor statistical agreement with the other results because of systematic errors arising from the cross-phase spectral contamination. The proposed method allows quantification to be performed in the presence of discontinuous phase distributions and overlapping phases, challenges that are typical of many nanoscale analyses performed by STEM-EDS.

© 2009 Elsevier B.V. All rights reserved.

1. Introduction

A spectrum image (SI, sometimes called a hyperspectral image), is a dataset produced by the acquisition and storage of full spectra at many spatially distinct points in a sample [1–3]. Typical materials science applications of spectrum imaging include secondary ion mass spectroscopy (SIMS) [4], proton-induced X-ray emission (PIXE) [5], and X-ray photoelectron spectroscopy (XPS) [6]. In electron microscopy, techniques commonly performed in a spectrum imaging mode include energy dispersive spectroscopy (EDS) [7,8], electron backscatter diffraction (EBSD) [9], cathodoluminescence (CL) [10], and electron energy loss spectroscopy (EELS) [2,3,11–13].

An important and growing application of scanning transmission electron microscopy (STEM)-EDS spectrum imaging is in the quantification of atomic species present at each pixel. Hunneyball et al. [14] produced the first quantitative STEM-EDS maps. Later authors [7,15–19] were able to push quantitative mapping to near-one-nanometer spatial resolution and very high chemical sensitivity. As shown by Watanabe et al. [20], using principal component analysis (PCA) [a type of multivariate statistical analysis (MVSA)] as a noise-filter allows very minor (<1 wt%) components to be examined at high spatial resolution (<5 nm), especially when combined with the very bright probe of an aberration-corrected cold-field-emission STEM. Following that work, we have recently used PCA noise-filtering to produce quantitative maps of cation fractions in (Pb,La)(Zr,Ti)O_3 (PLZT) thin-film materials [21].

Traditionally, quantitative STEM-EDS studies were performed by analyzing individual points, or a few points in a linescan [22], rather than quantifying pixel-by-pixel in a map or SI. These results

* Corresponding author.
E-mail address: parishcm@ornl.gov (C.M. Parish).
[1] Present address: Oak Ridge National Laboratory, Oak Ridge, TN 37831, USA.

0304-3991/$ - see front matter © 2009 Elsevier B.V. All rights reserved.
doi:10.1016/j.ultramic.2009.10.011

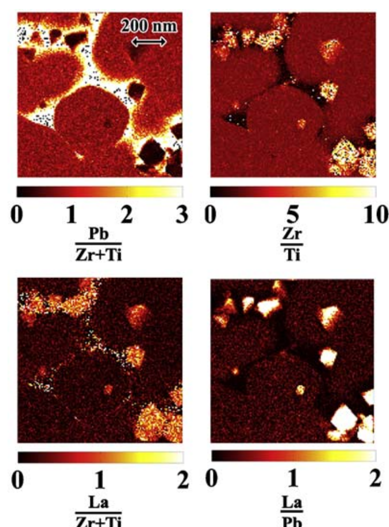

Fig. 1. Quantitative cation fraction ratio maps of sintered PLZT material. HAADF image is in Fig. 2a.

would be reported by quoting an atomic or weight fraction ratio with a specified statistical standard deviation or confidence limit, or by presenting the data as a graph of these ratios versus linescan position, along with error-bars on each datapoint denoting the uncertainty at that point. In general, the uncertainties associated with traditional STEM-EDS quantifications will be a combination of the Poisson counting statistics and the scatter in experimentally measured sensitivity factors. However, error analyses of quantitative STEM-EDS SIs have not been reported. Fig. 1 illustrates quantitative cation fraction maps of PLZT material; clearly, there is significant experimental scatter from one pixel to the next, even within the same phase, indicating that the precision and accuracy of such quantitative mapping is uncertain. In order for quantified STEM-EDS SIs to be truly quantitative, so as to interpret materials properties with respect to structure and phase diagrams, the accuracy and precision should be known.

The standard methods of calculating uncertainties in EDS quantifications are based on the Poisson statistics of the particle-counting nature of EDS detection. However, it is not clear a priori that the noise structure of a SI, after PCA processing, will be Poissonian in character. In particular, scaling for Poisson noise before PCA and the reconstruction of the point spectra from a small number of loading spectra may result in pixel-to-pixel variations that Poisson noise does not describe well. If we hypothesize that PCA-denoised SIs cannot be treated by standard error analysis, then a new means to extract the precision must be found.

Our goal in this paper is to determine statistical confidence bounds for STEM-EDS SI quantifications. The method we choose is to aggregate the raw SI data into individual phase spectra, because addition of Poisson variables maintains their Poissonian nature in the sum. We describe techniques to segment a STEM-EDS SI into individual constituent phases, and then use standard quantification techniques to calculate the chemistry and its associated confidence bound within each phase. Qualitative segmentation of spectrum images was suggested by Bonnet [23], and creating binary masks and summing the raw SI data under them has been reported previously by Kotula and Keenan [24], where it was used for qualitative analysis of interfacial segregation measured via STEM-EDS. Similar techniques have been used in SIMS [25] to determine phase volume fractions. The current results are extensions in that we then (1) perform a full quantitative analysis upon the obtained spectra and that (2) we compare different segmentation methods. We choose PLZT-based materials as our examples for several reasons. (1) Pb-based ferroelectric oxides can show instability under a bright electron beam [26–28], so the native short dwell times of SI techniques may be beneficial for quantification. (2) The example chosen here is not *spatially simple*; that is to say, a single pixel in the SI may contain more than one phase in the thickness of the TEM foil. This spatial non-simplicity will provide complications to test the applicability of the proposed method.

The proposed technique is advantageous over traditional methods, such as a point-analysis, because the dose is spread across a large sample area, and discontinuous regions of the same constituent phase can be aggregated together. The disadvantage is that pixels containing more than one phase will bias the results, and this must be accounted for; additionally, the extracted phase quantifications will be averaged across each phase, rather than indicative of a given point. This is also a step towards the eventual goal of a quantitative understanding of elemental composition and error propagation through the PCA and quantification procedures.

2. Experimental procedure

2.1. Ceramic processing

A ferroelectric thin-film of nominal composition $Pb_{0.88}La_{0.12}Zr_{0.70}Ti_{0.30}O_3$ (PLZT 12/70/30) is used as our example. The sample was produced by pressing and sintered chemically prepared precursor powders. The structure, as seen in Fig. 1, consists of a matrix of PLZT grains, with La–Zr rich precipitates and a Pb-rich film wetting many of the grain boundaries. The phases are referred to as “matrix,“ “precipitates,“ and “film” in this work.

2.2. Electron microscopy

Samples were prepared for STEM by milling in a FEI DB-235 dual-beam focused ion beam/scanning electron microscope (FIB/SEM) instrument, and were lifted out and placed on carbon-filmed copper grids. Primary milling was performed with a 30 keV gallium ion beam; finish milling was with a 5 keV gallium ion beam. STEM was performed in a Phillips Tecnai F30-ST Schottky emission TEM/STEM instrument operated at 300 keV, equipped with an EDS detector by EDAX.

Our SI quantification procedure is described in detail in our previous work [21], but we will summarize it here. For quantification of the cation contents, each individual pixel's spectrum was reconstructed from the significant principal components as a noise-filtering step; PCA is described in the next section. The reconstructed spectrum at each point was top-hat filtered to remove the background contribution [29–31]. The characteristic peaks (Pb L series, Zr K series, Ti K series, and La L series) were deconvolved and integrated by multiple linear least squares fitting of similarly filtered reference spectra to the experimental spectra [32]. Reference spectra were acquired from pure oxides PbO, ZrO_2, TiO_2, and La_2O_3. This step is necessary, in particular, to deconvolve the Ti K/La L overlap.

Once the integrated counts I_{Pb}, I_{Zr}, etc. were found at each pixel from the deconvolution procedure, the Cliff–Lorimer technique [33] was used to quantify the ratios of cations. The Cliff–Lorimer equation states that a ratio of chemical concentrations C_A/C_B for

elements A and B will be related to the integrated count ratio I_A/I_B via a sensitivity factor k_{AB}:

$$\frac{C_A}{C_B} = k_{AB}\frac{I_A}{I_B} \tag{1}$$

In our case, C_A, etc. are measured in terms of cation fraction. The k_{AB} factors were measured experimentally from crushed powder standards of $PbTiO_3$, $PbZrO_3$, and $Ti_2La_2O_7$, and whose spectra were integrated using identical techniques as the datapoints. From the assumption

$$C_{Pb}+C_{Zr}+C_{Ti}+C_{La}=1 \tag{2}$$

the cation fraction ratios can be converted to cation fraction. All integration and analysis was performed using MATLAB scripts.

Eq. (1) gives the value of a cation fraction ratio C_A/C_B at some point (x, y). The associated statistical standard deviation, $\Delta(C_A/C_B)$, is given by [34]

$$\Delta\left(\frac{C_A}{C_B}\right) = \left(k_{AB}\frac{I_A}{I_B}\right)\sqrt{\left(\frac{\sqrt{I_A}}{I_A}\right)^2+\left(\frac{\sqrt{I_B}}{I_B}\right)^2+\left[\frac{\Delta(k_{AB})}{k_{AB}}\right]^2} \tag{3}$$

Eq. 3 is based upon Poisson counting statistics where the variance is equal to the measurement, and assumes uncorrelated variances [35]. Here, $\sqrt{I_A}/I_A$ is the 1σ standard deviation in the peak A, and $\sqrt{I_B}/I_B$ is the 1σ standard deviation in the peak B. $\Delta(k_{AB})$ is the standard deviation in k_{AB}. Because k_{AB} is obtained from multiple measurements of a standard, $\Delta(k_{AB})$ is determined from a *t*-analysis of the multiple measurements [22,34]. Eq. (3) is written for 1σ, but higher standard deviation values could be incorporated easily. This equation is used to calculate error-bars and uncertainties below.

The Cliff–Lorimer equation assumes that the peaks I_A and I_B not be absorbed at different rates by the sample, which translates to a thin-foil assumption. As discussed elsewhere [21,36], in these

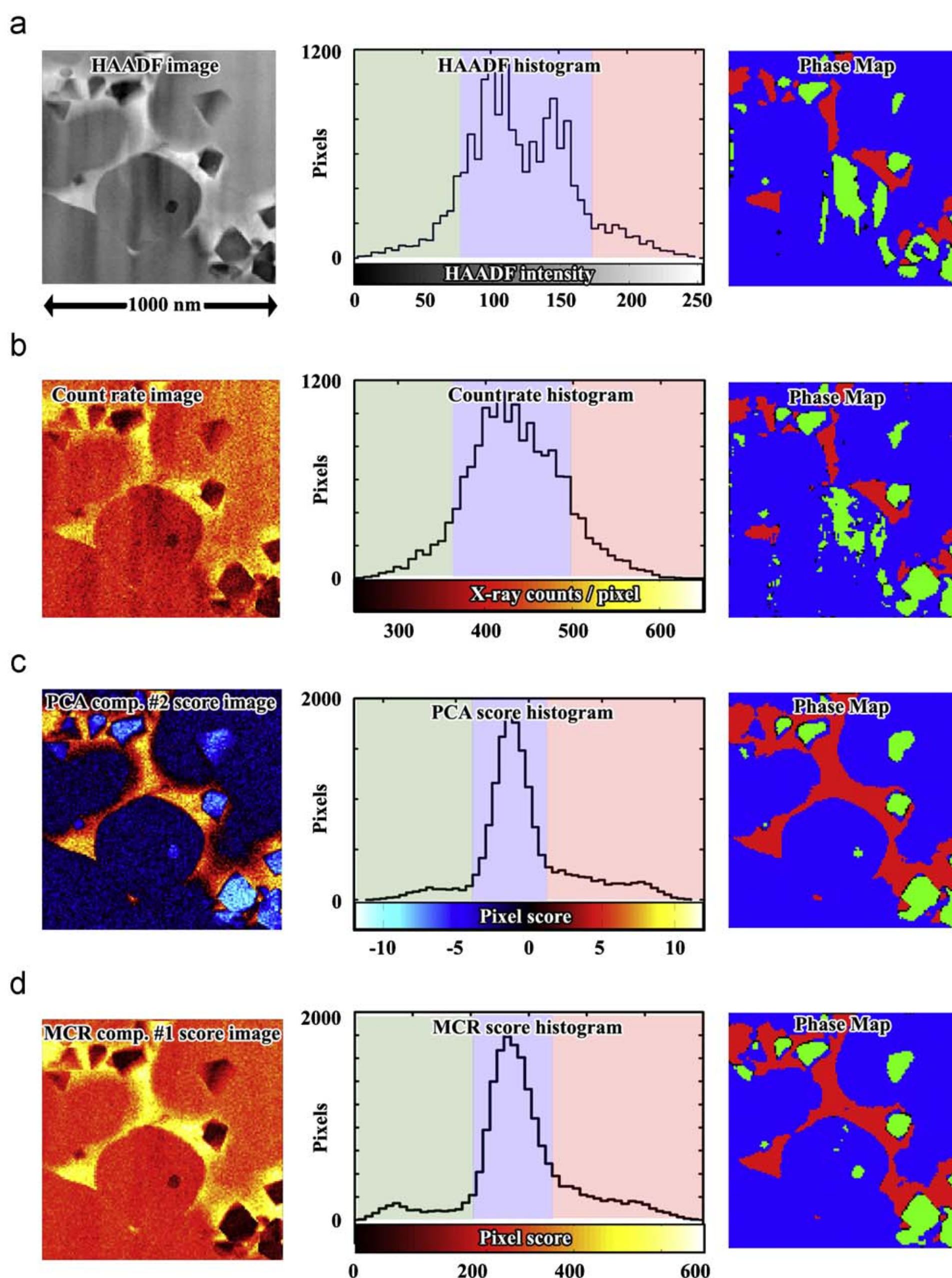

Fig. 2. Comparison of (a) HAADF, (b) count rate, (c) PCA and (d) MCR based segmenting of the sintered PLZT sample.

samples, the thin-foil assumption is met to better than 5%. Eq. (3) can only account for statistical, not systematic, errors. Systematic errors likely present in this work are (1) surface-Pb-depletion, particularly in the matrix phase, due to FIB-based sample preparation [36] and (2) differential absorption. When the relative error from Eq. (3) is ~3–5% or less, differential X-ray absorption in

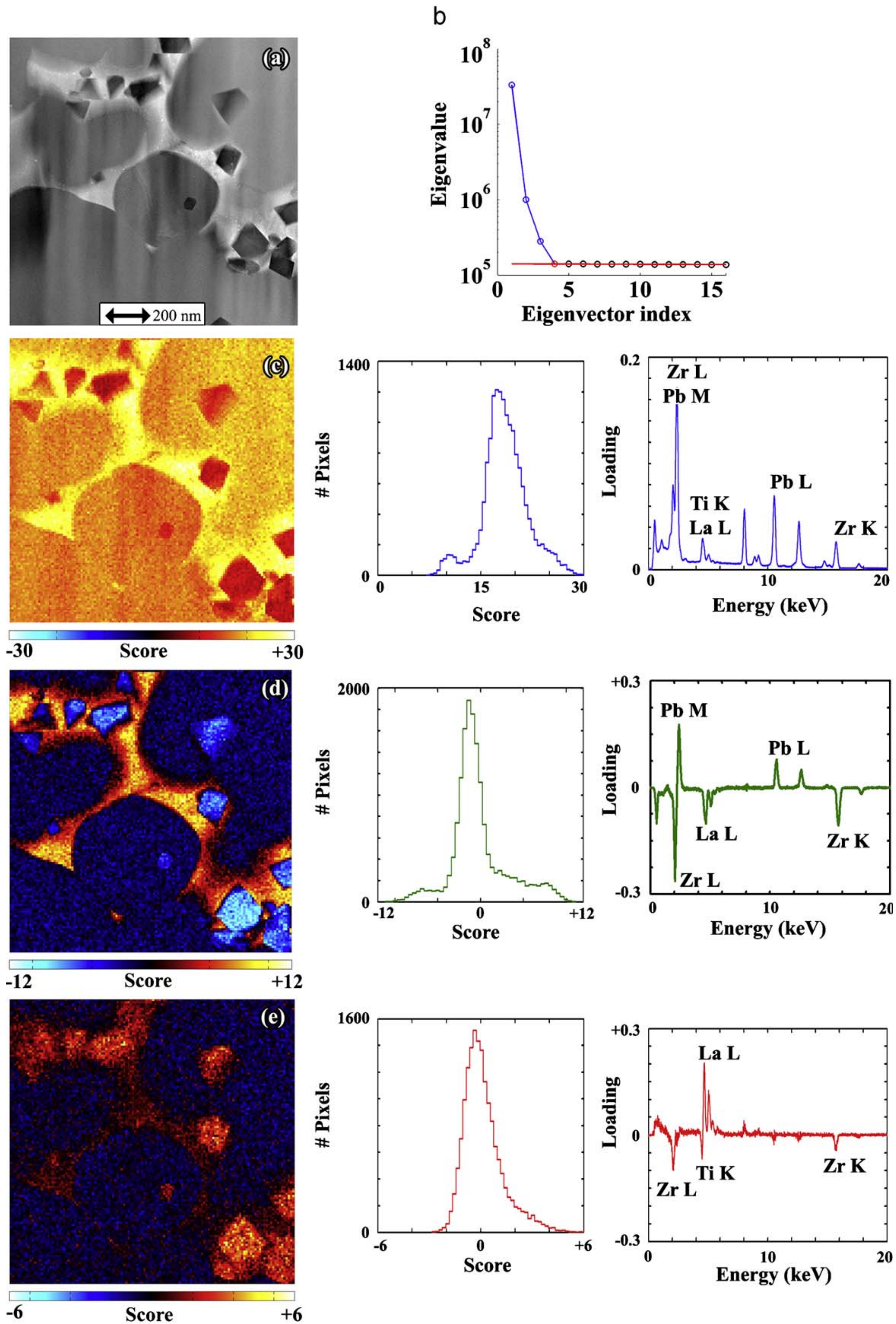

Fig. 3. (a) HAADF image, (b) Eigenvalue plot and (c–e) PCA components and score histograms of the sintered PLZT sample.

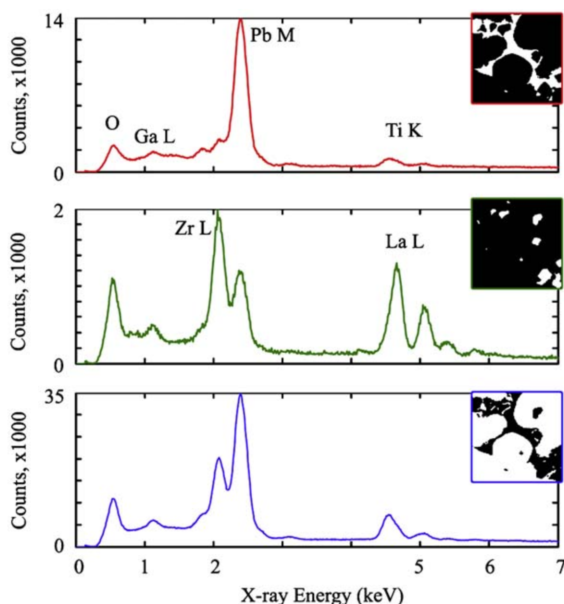

Fig. 4. Grain-boundary film (top), precipitate (middle) and matrix (bottom) summed spectra. Insets are the associated PCA-component derived phase mask (Fig. 2c).

the thin-film sample will likely dominate the statistical errors. Methods to account for thin-film differential absorption exist [15], but our emphasis in this paper is segmentation methods, so to avoid unnecessary complication we use the Cliff–Lorimer thin-foil method.

2.3. Principal component analysis (PCA)

The application of PCA to spectrum images has been described previously [11,19,37]. Because of the Poisson nature of the noise structure in EDS spectrum images, the SI data must be pre-processed using the "Optimal Scaling" method [38–40]. Otherwise, PCA will prefer to describe variance arising from noise in large peaks over small chemical features. This pre-processed, Poisson-scaled SI data is then subjected to PCA as described in detail by Keenan [37]. Following PCA analysis, the components describing noise are discarded, leaving only the components that carry chemical information. This result is then returned to physical space from Poisson-space by applying the inverse of the Poisson scaling [37]. These steps were performed using the software package "AXSIA" from Sandia National Laboratories [8]. Finally, the returned, physical-space components are reorthogonalized using the "fPCA" MATLAB method described by Keenan [37].

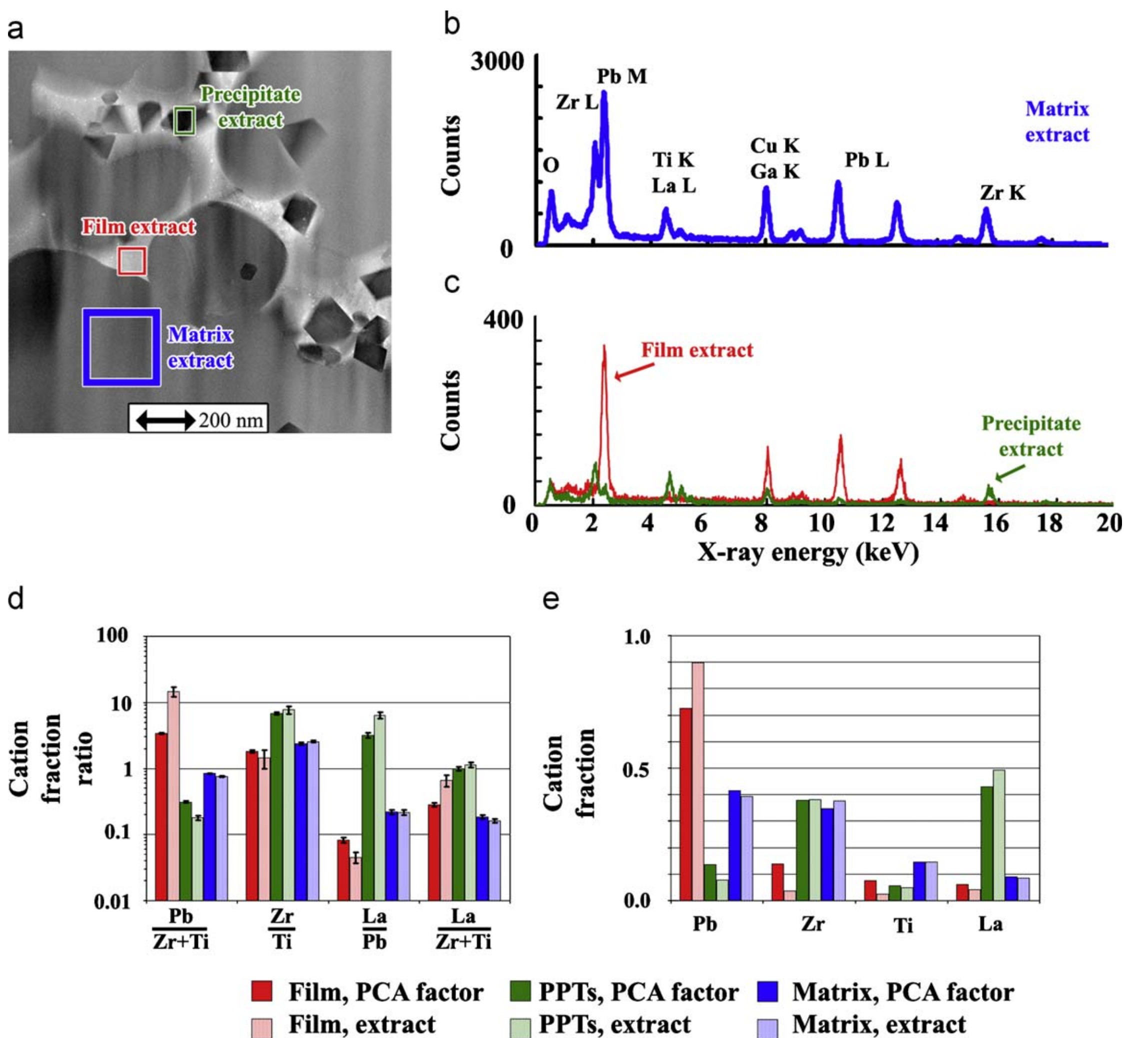

Fig. 5. (a) HAADF image. The colored boxes indicate manually-defined areas where the SI pixels were summed to provide (nominally) single-phase reference spectra. (b) and (c) Show these summed spectra. (d) Shows comparisons of the three phases quantified cation fraction ratios determined from PCA segmentation and the extracted areas in (a). (e) Comparison of the quantified cation fractions. Error bars in (d) are $\pm 2\sigma$. PPTs=precipitates.

A technique related to PCA is multivariate curve resolution, MCR. Non-negativity constrained MCR using alternating least squares is often applied to PCA solutions due to the abstract nature of the PCA scores and loadings. The MCR solution was also calculated using AXSIA [8,37,41,42].

3. Results and discussion

3.1. Initial results

In STEM, the high-angle annular dark-field (HAADF) image is very sensitive to the mass-thickness of the sample. We hypothesize HAADF intensity would be a possible means to assign segmentation of phases. Recall Fig. 1, which illustrates quantitative cation fraction ratio maps of the sintered PLZT sample. Fig. 2a shows the HAADF image of the sample, as well as a histogram of the HAADF intensity. The HAADF image was down-sampled to 128×128 pixels in order to match the size of the spectrum image. Also shown in Fig. 2a are a histogram of HAADF values and a derived segmented phase map. The phase map is determined by selecting areas in the HAADF image that have approximately the same gray-scale intensity, and then creating a mask from these values. Specifically, large changes in the histogram slope were chosen as the borders between phases. The colored boxes in the HAADF histogram indicate the HAADF pixel intensities that contributed to the phase mask. Green denotes the inclusions phase, red the grain-boundary film, and blue the matrix. (All phase maps presented in this work have had a "majority" morphological operation applied to them. The majority operation sets a pixel to "on" – i.e., red, green, or blue – if five or more of its neighboring nine pixels are the same color, and sets the pixel to "off" – black – otherwise. This removes isolated hot and cold pixels.)

Clearly, the HAADF signal is inappropriate and does a poor job of segmenting the phases in this case. Because this material is multi-phase and prepared by FIB, curtaining artifacts were visible in the HAADF image and resulted in thickness-based contrast that dominated the chemical contrast. Similarly, using the X-ray count rate at each pixel (Fig. 2b) provides essentially the same (incorrect) result.

PCA or MCR, however, are inherently multivariate methods and may be advantageous in comparison to inherently univariate methods such as the HAADF or count-rate imaging. Fig. 3 shows PCA results of the spectrum image. Fig. 3a shows the HAADF image and Fig. 3b the eigenvalue plot. The eigenvalue plot indicates a rank of 3 in the dataset. Figs. 3c–e show the three significant PCA components, along with score image histograms. The first component, Fig. 3c, is approximately the mean image and mean spectrum of the dataset. As such, segmentation of the first score image would give results similar to the count rate image (Fig. 2b). However, the second and third PCA components, Figs. 3d–e, carry the anti-mixing corrections and therefore their contrast arises primarily from chemical differences.

In Fig. 2c, we use the second PCA component to segment the image into three phases. The phase map in Fig. 2c matches much more closely the reality of the sample. For instance, segmenting of the HAADF or count-rate images misassigned the dark curtained matrix area near the center of the SI to precipitate (green) identity. The PCA-component mask correctly assigns this region to the matrix phase. Similarly, small isolated precipitates are properly extracted in the PCA-component phase mask, in contrast to the other methods. Fig. 2d shows a similar analysis from an MCR solution, and is very similar to the PCA result.

Fig. 4 shows the extracted spectra from each phase for the PCA-component phase mask. A single SI pixel would have a full-scale of 5–10 counts, typically. The summed spectra in Fig. 4 show 2000–35,000 counts full scale, indicating the magnitude of signal-to-noise increase achieved by segmentation. The count rate and

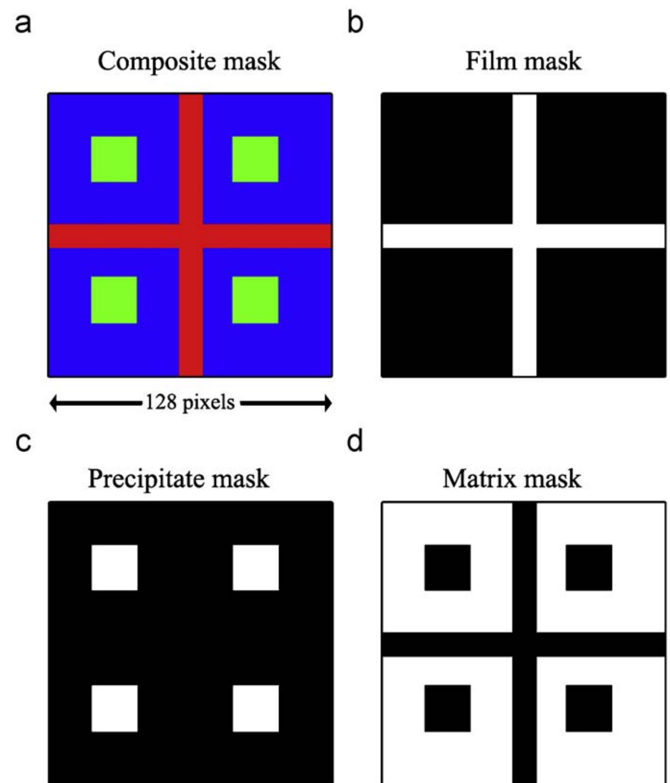

Fig. 6. (a) three-color composite phase-mask for the simulated spectrum image. (b–d) are the film, precipitate, and matrix components.

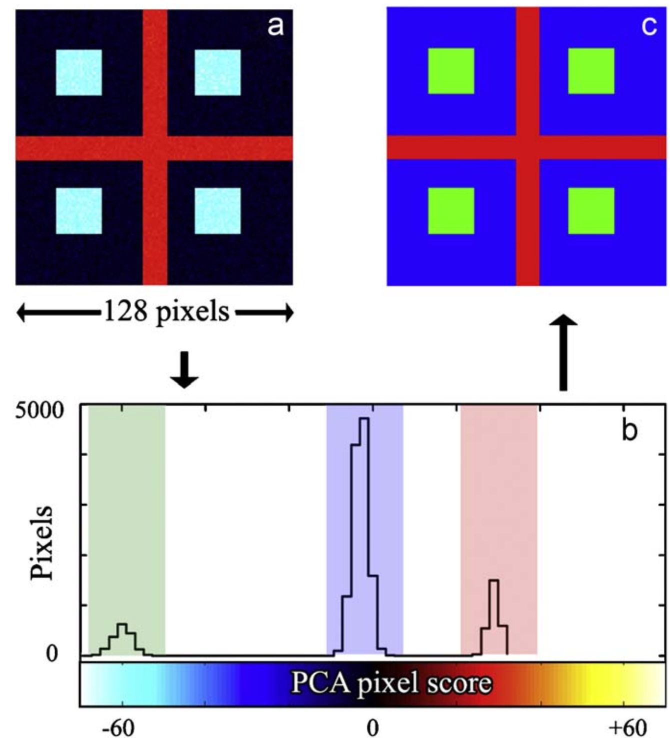

Fig. 7. 1000 count/pixel simulation results. (a) PCA-component score image of the simulation in Fig. 6. (b) Score-image histogram. (c) Re-created phase mask.

associated statistical bound will be best in phases with a large number of pixels as compared to phases with fewer associated pixels. Results for the MCR-derived phase mask are essentially the same as those for the PCA phase mask, although the film-phase derived via MCR shows slightly higher Pb-content than the film-phase derived via PCA.

Fig. 5 allows us to make a comparison of the PCA-component segmentation method to more traditional quantification methods. (The MCR-component segmentation would be substantially similar and is omitted for brevity.) In Fig. 5a, three colored boxes are marked around areas that *appear* to be single phase. The SI pixels within each box are summed, producing the spectra in Fig. 5b (matrix) and Fig. 5c (film and precipitate). Fig. 5d compares the quantified cation fraction ratios for the two methods (extraction and PCA-component segmentation) for each of the three phases. Fig. 5e shows the quantified cation fraction data. The error bars in Fig. 5d are $\pm 2\sigma$.

The results in Fig. 5d show that the PCA-component and extract quantifications for the matrix phase are within the statistical bounds, indicating good agreement. However, the film and precipitate phase quantifications do not agree well.

3.2. Comparison to simulations

In order to interpret these results, we have performed a series of simulations. EDS spectra were simulated using the software DTSA-II, by Ritchie at the National Institute of Standards and Technology (USA) [43]. Spectra were simulated assuming a 300 keV electron beam, a 10 nm thick foil, and a 20° take-off angle to an ultra-thin window detector. Detector resolution of 200 eV Mn Kα was assumed, which closely matches the experimental resolution of our detector under fast-mapping conditions. Although the present implementation of DTSA-II is intended for SEM rather than (S)TEM simulations, the simulated spectra are physical in appearance and suit the purposes of our approximations quite well. The film phase was simulated assuming $Pb_{0.9}La_{0.03}Zr_{0.03}Ti_{0.03}O$ stoichiometry. The precipitate phase was $ZrLaO_2$, and the matrix phase was $Pb_{0.88}La_{0.12}Zr_{0.70}Ti_{0.30}O_3$. These simulated stoichiometries are meant to be illustrative, rather than exact replications of the phases present in the experimental sample. Fig. 6 illustrates the 128×128 pixel masks for the first simulation.

In this first simulation, the three phases are assumed to be full-thickness through the foil and to show no mixing at the boundaries; in other words, perfect spatial simplicity. The SI was populated with simulated spectra according to the phase mask, and then Poisson noise was added to each pixel at a noise level of 1000 mean counts/pixel. Fig. 7 shows the results of application of our techniques to this simulation. Fig. 7a is the second PCA component's score image, and is qualitatively similar to that seen in Fig. 2c. Fig. 7b shows the score histogram, along with colored boxes denoting the pixels assigned to each phase

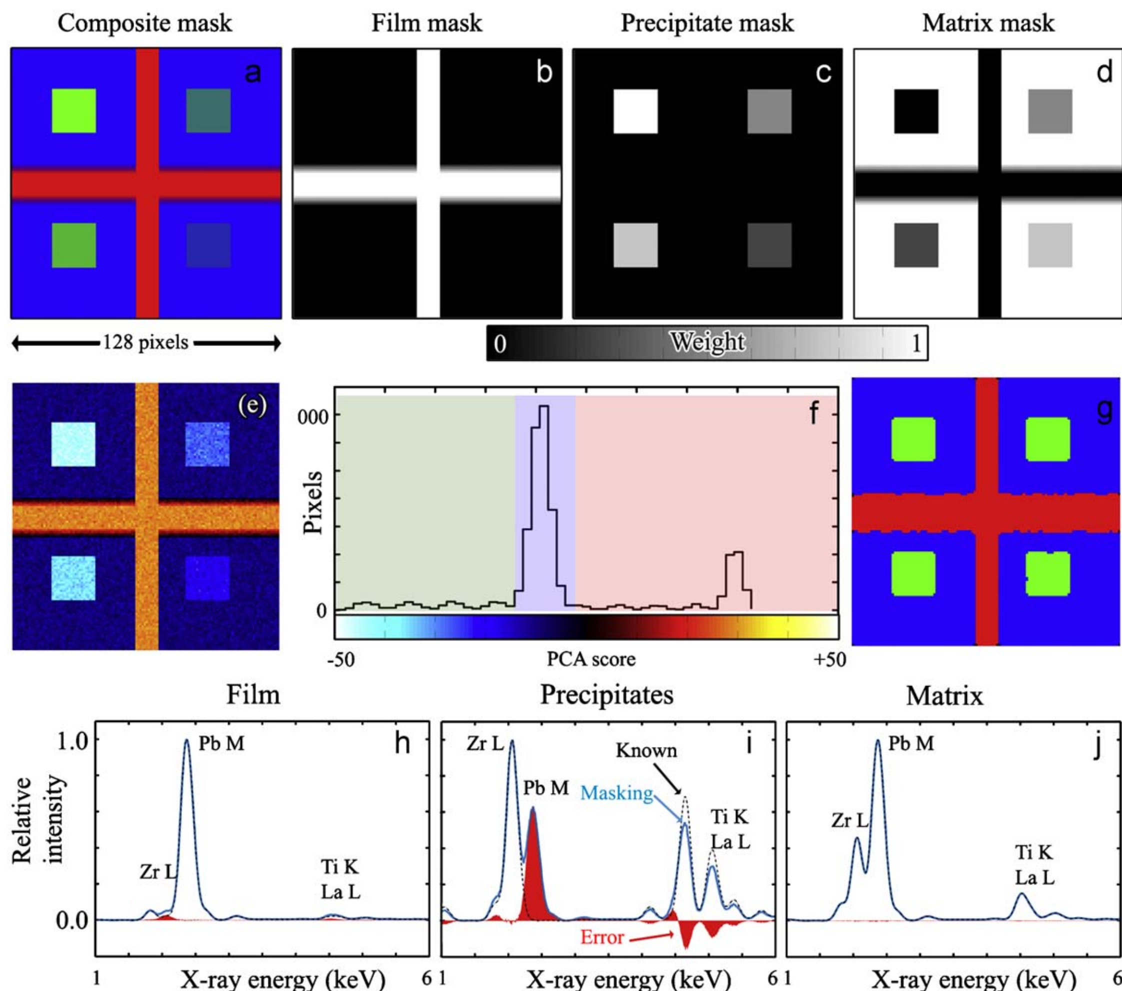

Fig. 8. (a) Composite masks and (b–d) individual phase masks used for simulation starting point. (e) PCA component-2 score image for the analyzed simulation at 1,000 base counts/pixel. (f) Score image histogram. (g) Derived phase mask. (h–j) Comparison of mask-derived aggregated spectra to the known starting spectra. The error is shown in red. For interpretation of the references to colour in this figure legend, the reader is referred to the web version of this article.

mask in Fig. 7c. The phase mask perfectly replicates the starting mask of Fig. 6a. Comparison of the summed spectra within each phase mask show residuals $<2\%$ different from the starting spectra.

This leads to the conclusion that in a spatially simple sample without sub-thickness inclusions or tilted boundaries, the proposed segmentation method will correctly recreate the original structure.

However, a real STEM sample will not be spatially simple. Fig. 8a shows a composite mask for a non-spatially simple simulation. Figs. 8b–d show the individual phase masks used for the starting point of the simulation. In Figs. 8b and d, the film and matrix meet at either sharp or tilted interfaces. There are four precipitates in the simulation (Fig. 8c). One is full thickness, one 75%, one 50%, and one 25%. The remainder of the thickness around the precipitate is matrix phase.

Because the three phases in the experimental sample have strongly different compositions, they exhibit different count rates in EDS. Thus, in this simulation, the base count rate for a matrix pixel was kept at 1000 counts, the count rate for a film pixel was 1250 counts, and for the precipitates 750 counts. Fig. 8e shows the PCA component-2 score image and Fig. 8f the score histogram. This score histogram again qualitatively resembles the experimental histogram in Fig. 2c, although it is different in fine detail. Defining the mask in a manner similar to the experimental case gives the composite mask shown in Fig. 8g. The binary nature of the mask results in inconsistencies when compared to the known starting point, Fig. 8a.

The aggregated spectra are compared to the known starting spectra in Figs. 8h–j. The matrix spectrum (Fig. 8j) agrees almost perfectly, differing only by random noise. The film spectrum (Fig. 8h) differs slightly, with variations at the Zr, Ti, and La lines. However, the precipitate aggregated spectrum (Fig. 8i) is quite incorrect. The precipitate spectrum should only contain Zr and La, but shows large Pb and Ti contributions, which come from mixing with the matrix in the non-full-thickness precipitate regions.

With this knowledge, we can then re-define the regions of the histogram that contribute to the composite phase mask for aggregation. Fig. 9a shows the same score histogram, but with differently defined mask regions. The resulting mask is in Fig. 9b. It can be seen that the tilted regions of the film and the non-through-thickness precipitates are neglected. Which is to say, black pixels in the composite mask are spatially mixed and excluded from the analysis. The advantage of discarding the spatially mixed pixels in seen in Fig. 9c, where the known and aggregated precipitate spectra differ only by random noise, with no systematic component. (The film and matrix behave similarly and are omitted for brevity.) The disadvantage to discarding the mixed pixels is that overall signal levels are reduced, resulting in larger error-bars. We can now attempt to apply this insight by re-analyzing the experimental data.

3.3. Refined results

As noted above (Section 3.1), the comparisons of manually extracted spectra to those found from PCA-component based segmentation and aggregation agreed for the matrix phase, but not for the film or precipitate phases (Fig. 5d). The simulated results (Section 3.2) indicate that discarding the non-spatially simple pixels may assist in the extraction of aggregated spectra that more faithfully replicate the "true" chemical composition of

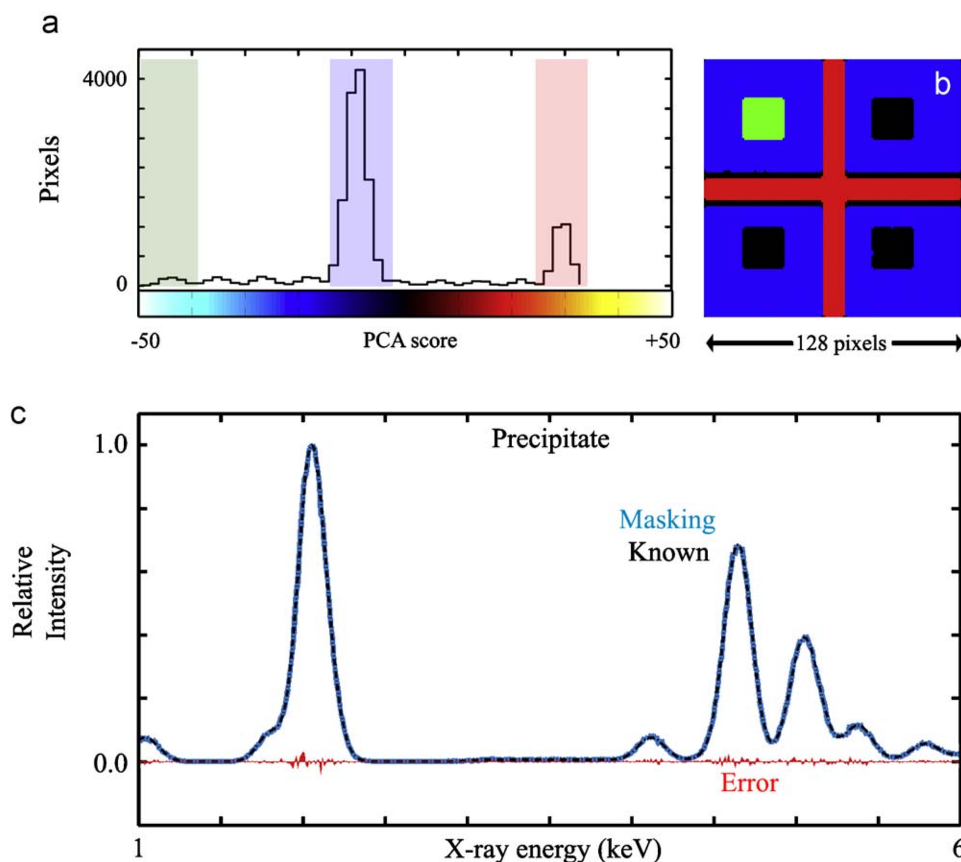

Fig. 9. (a) Score image histogram with re-defined limits. (b) New composite mask. (c) New aggregated spectrum compared to the known spectrum. Error is in red. For interpretation of the references to colour in this figure legend, the reader is referred to the web version of this article.

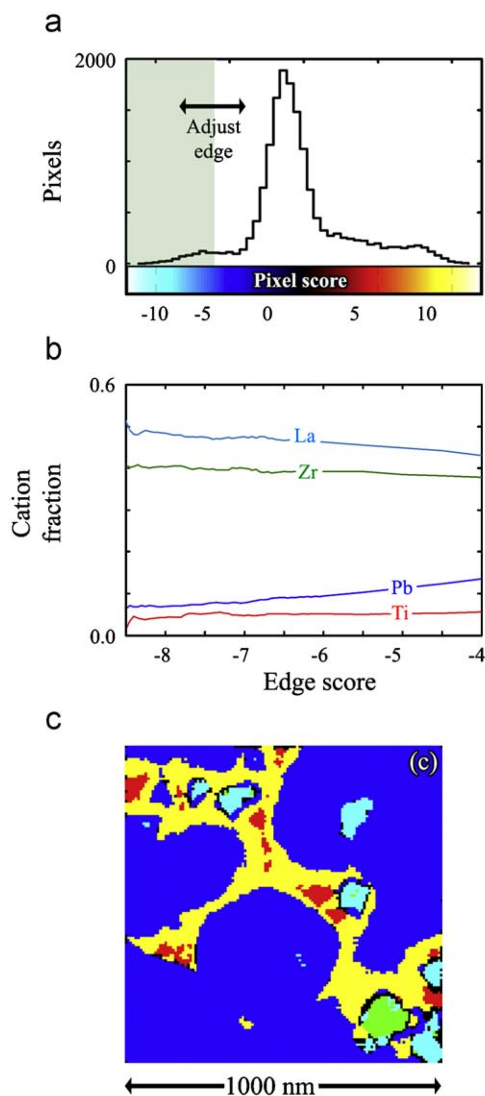

Fig. 10. (a) PCA score histogram, showing adjustment of the precipitate region. (b) Quantified cation fractions vs. the score of the upper edge of the histogram region. (c) Final phase map. Precipitate: green; film: red; matrix: blue; excluded precipitate: cyan; excluded film: yellow. For interpretation of the references to colour in this figure legend, the reader is referred to the web version of this article.

the constituent phase, although with poorer counting statistics. However, a realistic experimental sample has a score histogram that is much more complicated than that for the simplified simulation, so it will be more difficult to properly decide where to place the phase-boundaries in the histogram.

We suggest that the edge of the region can be varied systematically, and quantities such as the number of pixels in the associated mask, or the cation fractions quantified by aggregating the signal under the mask, can be plotted vs. the edge value. In Fig. 10a, we illustrate this approach for the precipitate phase defined via PCA score histogram. (In a sample where HAADF, count-rate images, MCR score images, or other techniques provided better segmentation, those histograms could be used just as easily.) In Fig. 10b the cation fractions are calculated as a function of upper edge value. (The lower edge is fixed.) The quantified cation fractions appear to plateau from -7 to -8 in upper edge score. (The MCR results can also be examined in this same fashion; the differences between MCR and PCA are minor, so we omit the MCR results.) Thus, we can select a value of -7 for the upper edge score. The boundary for the film phase can be selected similarly. Fig. 10c shows the final derived phase mask; cyan pixels are nominally precipitate phase that has been excluded, and yellow pixels nominally film phase that has been excluded. The quantifications are shown in Fig. 11, and compared to the extracted quantifications shown in Fig. 5.

The refined phase-mask results compare much more closely to the extracted data quantifications. Although the La/Pb and La/(Zr+Ti) cation fraction ratios in the film phase does not agree between the two methods, all of the other ratios are within the error bars. However, as more pixels are discarded in order to eliminate the non-spatially simple pixels, the aggregate signal levels are reduced, which results in larger statistical errors, and concomitant broadening of the error bars in Fig. 11 as compared to Fig. 5. However, we suggest that the improved accuracy outweighs this loss of precision.

It is possible that none of the precipitates are through-thickness, and therefore no spatially simple solution exists. If so, this is a problem that could be avoided by using a thinner area of the sample, although a thin area will result in reduced X-ray count rates and concomitantly increased uncertainty in all measurements.

4. Conclusions

Quantification of STEM-EDS SIs is a rapidly developing technique. However, the use of multivariate statistical analysis may invalidate traditional means of measuring the precision of such quantifications. Here, we proposed masking and aggregation techniques to obtain quantitative chemical analyses and associated error analysis from STEM-EDS SIs. PCA or MCR methods were found to be superior to HAADF or count-rate signals for assigning segmentation. This aggregation technique provides a result conceptually the same as would be obtained by dwelling a STEM beam on a sample area for seconds or minutes, and then quantifying the resulting spectrum. However, three advantages are apparent with the proposed method compared to the long-dwell method:

(1) The dwell time per point is very short in a spectrum image (100 ms/pixel in these experiments). This will minimize localized beam damage or contamination that might bias the results of a longer-dwell-time acquisition.
(2) The aggregation of pixels from a single phase does not require any sort of continuity or even proximity. In the case of the inclusions, the aggregated spectrum is accumulated from many small, spatially distinct regions in the specimen that would be difficult to access or aggregate without a masking technique.
(3) By using PCA or MCR, the multivariate analysis of the compositional signal itself determines the boundaries of different constituent phases through the score-image histograms; the boundaries are not assigned *a priori*.

Comparison of the proposed method to a more traditional analysis showed that spatial-non-simplicity of the experimental sample resulted in systematic bias of the aggregated results. However, a combination of Monte Carlo simulations and systematic analysis of the experimental data showed that the proposed technique can well-replicate a more traditional result while maintaining the advantages (1–3) enumerated above. The results presented in this work discuss the segmentation of the spectrum image in the spatial domain. We intend to later present a follow-up publication that discusses segmentation within the spectral domain.

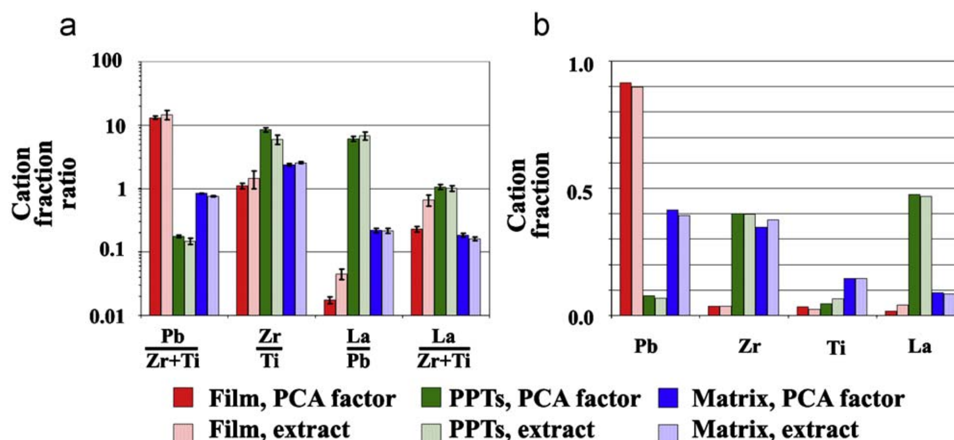

Fig. 11. Quantified (a) cation fraction ratios and (b) cation fractions for the extracts and the final PCA-component derived phase masks. Error bars in (a) are $\pm 2\sigma$.

Acknowledgements

Sandia is a multiprogram laboratory operated by Sandia Corporation, a LockheedMartin Company, for the United States Department of Energy's National Nuclear Security Administration under contract DE-AC04-94AL85000. Bruce Tuttle and Pat Mahoney provided the PLZT samples. Mike Keenan, Paul Kotula, Chris Stork, Blythe Clark, and Khalid Hattar provided comments and discussion.

References

[1] J.J. Friel, C.E. Lyman, Microscopy and Microanalysis 12 (2006) 2–25.
[2] J.A. Hunt, D.B. Williams, Ultramicroscopy 38 (1991) 47–73.
[3] C. Jeanguillaume, C. Colliex, Ultramicroscopy 28 (1989) 252–257.
[4] B. Tyler, Applied Surface Science 203 (2003) 825–831.
[5] B.L. Doyle, P.P. Provencio, P.G. Kotula, A.J. Antolak, C.G. Ryan, J.L. Campbell, K. Barrett, Nuclear Instruments & Methods in Physics Research Section B—Beam Interactions with Materials and Atoms 249 (2006) 828–832.
[6] D.E. Peebles, J.A. Ohlhausen, P.G. Kotula, S. Hutton, C. Blomfield, Journal of Vacuum Science & Technology A 22 (2004) 1579–1586.
[7] M.G. Burke, M. Watanabe, D.B. Williams, J.M. Hyde, Journal of Materials Science 41 (2006) 4512–4522.
[8] P.G. Kotula, M.R. Keenan, J.R. Michael, Microscopy and Microanalysis 9 (2003) 1–17.
[9] L.N. Brewer, P.G. Kotula, J.R. Michael, Ultramicroscopy 108 (2008) 567–578.
[10] P.R. Edwards, R.W. Martin, K.P. O'Donnell, I.M. Watson, Physica Status Solidi C 0 (2003) 2474–2477.
[11] P. Trebbia, N. Bonnet, Ultramicroscopy 34 (1990) 165–178.
[12] M. Bosman, M. Watanabe, D.T.L. Alexander, V.J. Keast, Ultramicroscopy 106 (2006) 1024–1032.
[13] P. Harkins, M. MacKenzie, A.J. Craven, D.W. McComb, Micron 39 (2008) 709–716.
[14] P.D. Hunneyball, M.H. Jacobs, T.J. Law, in: G.W. Lorimer, M.H. Jacobs, P. Doig (Eds.), Quantitative Microanalysis with High Spatial Resolution, The Metals Society, London, 1981, pp. 195–202.
[15] M. Watanabe, D.B. Williams, Journal of Microscopy 221 (2006) 89–109.
[16] D.B. Williams, A.J. Papworth, M. Watanabe, Journal of Electron Microscopy 51 (2002) S113–S126.
[17] E.P. Gorzkowski, M. Watanabe, A.M. Scotch, H.M. Chan, M.P. Harmer, Journal of Materials Science 39 (2004) 6735–6741.
[18] J.I. Goldstein, R.H. Jones, P.G. Kotula, J.R. Michael, Meteoritics and Planetary Science 42 (2006) 913–933.
[19] J.M. Titchmarsh, S. Dumbill, Journal of Microscopy—Oxford 184 (1996) 195–207.
[20] M. Watanabe, D.W. Ackland, A. Burrows, C.J. Kiely, D.B. Williams, O.L. Krivanek, N. Dellby, M.F. Murfitt, Z. Szilagyi, Microscopy and Microanalysis 12 (2006) 515–526.
[21] C.M. Parish, G.L. Brennecka, B.A. Tuttle, L.N. Brewer, Journal of the American Ceramic Society 91 (2008) 3690–3697.
[22] J.I. Goldstein, D.B. Williams, G. Cliff, in: D.C. Joy, A.D. Romig Jr., J.I. Goldstein (Eds.), Principles of Analytical Electron Microscopy, Plenum, New York, 1986, pp. 155–217.
[23] N. Bonnet, in: G.W. Bailey, R.V.W. Dimlich, K.B. Alexander, J.J. McCarthy, T.P. Pretlow (eds.), Microscopy and Microanalysis, Springer, Clevland, OH, 1997, pp. 929–930.
[24] P.G. Kotula, M.R. Keenan, Microscopy and Microanalysis (2006) 538–544.
[25] J.L.S. Lee, I.S. Gilmore, M.P. Seah, Surface and Interface Analysis 40 (2008) 1–14.
[26] M. Huffman, J.P. Goral, M.M. Al-Jassim, C. Echer, Journal of Vacuum Science & Technology A—Vacuum Surfaces and Films 10 (1992) 1584–1591.
[27] I. Reaney, D.J. Barber, Journal of Microscopy 160 (1990) 213–224.
[28] I.M. Reaney, K. Brooks, R. Klissurska, C. Pawlaczyk, N. Setter, Journal of the American Ceramic Society 77 (1994) 1209–1216.
[29] I.P. Jones, Chemical Microanalysis using Electron Beams, Institute of Metals, Bournemouth, 1992.
[30] D.B. WilliamsPractical Analytical Electron Microscopy in Materials Science, Philips Electron Instruments, Mahwah, 1984.
[31] F.H. Schamber, in: T.G. Dzubay (ed.), X-ray Fluorescence Analysis of Environmental Samples, Ann Arbor Scientific Publishers, Ann Arbor, 1977, pp. 241–257.
[32] J.I. Goldstein, D.E. Newbury, P. Echlin, D.C. Joy, A.D. Romig, C.E. Lyman, C. Fiori, E. Lifhsin, in: Scanning Electron Microscopy and X-Ray Microanalysis, Second ed., Plenum, New York, 1992.
[33] G. Cliff, G.W. Lorimer, Journal of Microscopy 103 (1975) 203–207.
[34] D.B. Williams, C.B. Carter, Transmission Electron Microscopy, Plenum, New York, 1996.
[35] P.R. Bevington, Data Reduction and Error Analysis for the Physical Sciences, McGraw-Hill, New York, 1996.
[36] C.M. Parish, G.L. Brennecka, B.A. Tuttle, L.N. Brewer, Journal of Materials Research 23 (2008) 2944–2953.
[37] M.R. Keenan, in: H.F. Grahn, P. Geladi (Eds.), Techniques and Applications of Hyperspectral Image Analysis, John Wiley & Sons, Chichester, 2007, pp. 89–126.
[38] M.R. Keenan, Journal of Vacuum Science & Technology A 23 (2005) 746–750.
[39] M.R. Keenan, P.G. Kotula, Surface and Interface Analysis 36 (2004) 203–212.
[40] M.R. Keenan, P.G. Kotula, Applied Surface Science 231-232 (2004) 240–244.
[41] M.R. Keenan, Surface and Interface Analysis 41 (2009) 79–87.
[42] M.H. Van Benthem, M.R. Keenan, Journal of Chemometrics 18 (2004) 441–450.
[43] N.W.M. Ritchie, DTSA-II, V.1.665, National Institute of Standards and Technology, 2008.